

# Downscaling Neural Network for Coastal Simulations

Zhi-Song Liu<sup>a</sup>, Markus Büttner<sup>b</sup>, Vadym Aizinger<sup>b</sup>, Andreas Rupp<sup>c</sup>

<sup>a</sup>*Department of Computational Engineering, Lappeenranta-Lahti University of Technology LUT, Lahti, Finland*

<sup>b</sup>*University of Bayreuth, Bayreuth, Germany*

<sup>c</sup>*Saarland University, Saarbrücken, Germany*

---

## Abstract

Learning the fine-scale details of a coastal ocean simulation from a coarse representation is a challenging task. For real-world applications, high-resolution simulations are necessary to advance understanding of many coastal processes, specifically, to predict flooding resulting from tsunamis and storm surges. We propose a Downscaling Neural Network for Coastal Simulation (DNNCS) for spatiotemporal enhancement to efficiently learn the high-resolution numerical solution. Given images of coastal simulations produced on low-resolution computational meshes using low polynomial order discontinuous Galerkin discretizations and a coarse temporal resolution, the proposed DNNCS learns to produce high-resolution free surface elevation and velocity visualizations in both time and space. To efficiently model the dynamic changes over time and space, we propose grid-aware spatiotemporal attention to project the temporal features to the spatial domain for non-local feature matching. The coordinate information is also utilized via positional encoding. For the final reconstruction, we use the spatiotemporal bilinear operation to interpolate the missing frames and then expand the feature maps to the frequency domain for residual mapping. Besides data-driven losses, the proposed physics-informed loss guarantees gradient consistency and momentum changes. Their combination contributes to the overall 24% improvements in Root Mean Square Error (RMSE). To train the proposed model, we propose a novel coastal simulation dataset and use it for model optimization and evaluation. Our method shows superior downscaling quality and fast computation compared to the state-of-the-art methods.

*Keywords:* Coastal simulation, deep neural networks, discontinuous Galerkin method, shallow water equations, downscaling.

---

## 1. Introduction

The two-dimensional shallow-water equations (SWE) can be utilized to model circulation in the global, regional, and coastal ocean, inland seas, lakes, and rivers; they are also frequently employed for atmospheric circulation studies [72]. Currently, SWE-based numerical software packages are the main tool employed in the operational forecast of tsunamis and storm surges [16, 5, 79, 17]. For many coastal ocean applications—flooding simulations are one crucial example—the accuracy of the model results strongly depends on the resolution of the computational mesh and the accuracy of the time discretization. To reliably meet the requirements of accurate prediction of inundation with the purpose of warning and hazard management, mesh resolutions down to and even below 10m in the affected areas [10] are necessary. Even using unstructured scenario-adapted meshes and GPU computing [55, 63], such resolution requirements are computationally challenging—especially in real-time warning systems [56].

Since coastal ocean simulations are important and challenging, they have been a focus of many research efforts resulting in numerous numerical and algorithmic advances in recent years. While many established software packages rely on Finite Volume of Finite Difference methods, the discontinuous Galerkin (DG) and other related discretization techniques (such as enriched Galerkin or hybridized DG methods) emerged in the last two decades as strong candidates, especially for unstructured mesh and adaptive simulations. For example, [24] derives an *hp* adaptive DG discretization, [15, 62] develop hybridized DG methods and suitable time-stepping approaches, whereas [39] proposes an adaptive enriched Galerkin scheme. A multiwavelet approach is explored in [32], while [36] further enhances the concept of adaptivity by omitting computations in the subdomain parts, where no changes take place.

Recently, there have been rapid developments of deep learning based super-resolution in image and video processing [85, 75, 76, 52]. The ill-posed problems in image processing are considered to be similar to the downscaling problem in scientific modeling, like fluid dynamic simulation [66], climate downscaling [7], and smoke simulation [8]. However, there are no or very few works on applying deep learning approaches for coastal ocean downscaling. This work exploits deep learning as an alternative for high-resolution (HR) shallow water models. Specifically, we propose a Downscaling Neural Network for Coastal Simulations (DNNCS) to downscale the results of low-resolution (LR) coastal simulations to obtain HR results. The overall

process is shown in Figure 1. We convert the coarse simulations of the target coastal model into three views: the horizontal depth-integrated horizontal velocity field ( $U, V$ ) and the water height ( $\xi$ ). Then, we merge them as RGB image inputs to the proposed DNNCS for downscaling. The super-resolved outputs can be used in place of fine-resolution simulations, e.g., to visualize the results. Besides the fast computation for HR shallow water simulations, another major advantage of our approach compared to other ML-based techniques is the fact that the coarse-resolution image originates from the numerical model and conforms to all physical constraints (in particular, the coarse-resolution solution is mass conservative), preventing the reconstructed fine-resolution solution from ‘drifting’ away from physical consistency for arbitrarily long simulation runs.

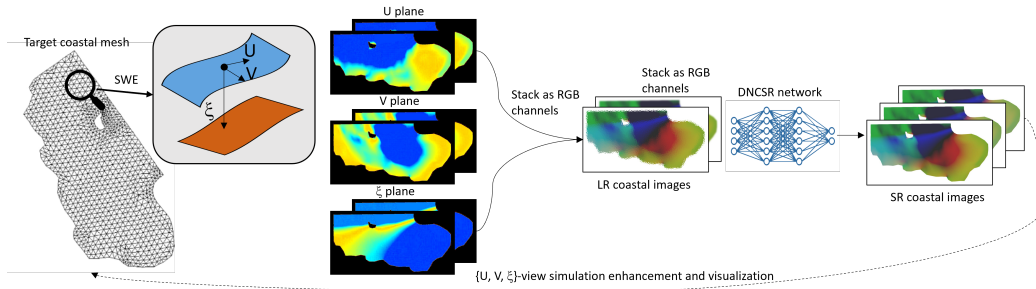


Figure 1: **The overall deep learning pipeline for coastal ocean downscaling.** We use the numerical model to simulate the coarse solution representation as  $U, V, \xi$ . We stack them as RGB channels to form a low-resolution (LR) image, which will be taken as input to the proposed DNNCS for spatiotemporal upsampling. The obtained downscaling coastal images seamlessly enhance the spatial and temporal details, which will be useful for coastal ocean simulation and visualization.

To summarize, our main contributions are as follows:

- We present a novel DNNCS for coastal ocean simulation, capable of efficiently generating high-resolution data and reducing the computational burden associated with PDE-based physical modeling.
- We introduce a spatio-temporal attention mechanism to jointly learn spatial and temporal downscaling, incorporating coordinate information as positional signals for grid-aware reconstruction.

- To ensure physical consistency, we incorporate physics-informed loss functions as constraints, guiding the model to produce reliable high-resolution outputs.
- We construct a new coastal simulation dataset featuring multiple levels of resolution to support effective model training and validation.

## 2. Governing equations and simulation software

Our governing equations are the 2D SWE in a conservative form on a 2D domain  $\Omega$  given by

$$\partial_t \xi + \nabla \cdot \mathbf{q} = 0, \quad (1a)$$

$$\partial_t \mathbf{q} + \nabla \cdot \left( \frac{\mathbf{q}\mathbf{q}^T}{H} \right) + \tau_{\text{bf}} \mathbf{q} + \begin{pmatrix} 0 & -f_c \\ f_c & 0 \end{pmatrix} \mathbf{q} + gH \nabla \xi = \mathbf{0}. \quad (1b)$$

Here,  $\mathbf{q} := (U, V)^T$  denotes the depth-integrated horizontal velocity,  $\xi$  the water elevation above some datum (e.g., the mean sea level),  $h_b$  the bathymetric depth respective the same datum, and  $H := h_b + \xi$  the total water depth. The other terms have the following meaning:  $f_c$  is the Coriolis coefficient,  $g$  is the gravitational acceleration, and  $\tau_{\text{bf}}$  is the bottom friction coefficient.

The boundary conditions relevant to our scenario are the land boundary condition  $\mathbf{q} \cdot \mathbf{n} = 0$  and the open sea boundary condition  $\xi = \hat{\xi}$ , which prescribes the tidal elevation at open sea boundaries given as a space- and time-dependent function  $\hat{\xi}$ .

The discretization of the SWE system defined in (1) using the discontinuous Galerkin (DG) method was initially realized in a code called UTBEST [1], which uses unstructured triangular meshes with DG polynomial approximations of orders zero (piecewise constant), one (piecewise linear), or two (piecewise quadratic). The time discretization is performed via explicit strong stability preserving Runge–Kutta methods [21] of orders one (explicit Euler), two, and three chosen in accordance to the spatial discretization.

The original UTBEST scheme proved very successful and has been further developed and transferred to several code development frameworks such as Matlab/GNU Octave [39], EXASTENCILS code generation framework [26, 4, 27, 25], OpenCL [44, 28], or SYCL [18, 19]. UTBEST also served as a basis for a fully-featured 3D regional ocean model UTBEST3D [22, 2].

### 3. Related Works

High-resolution coastal ocean simulation is important for accurately representing complex circulation—particularly relevant in the presence of irregular coastlines and strongly varying topography. However, simulating shallow-water equations at high spatial and temporal resolution requires massive computational efforts. To upsample the low-resolution (LR) scientific data to high-resolution (HR) full-field dynamics is called super-resolution (SR) in image and video processing, and downscaling in climate and weather prediction. Let us revisit related topics in two categories: deep learning for image/video super-resolution and physics-informed downscaling.

#### *3.1. Learning based super-resolution and downscaling*

Image and video super-resolution is an ill-posed problem. One LR image can lead to multiple plausible sharp and clean HR images. The typical solution is to use paired LR-HR data to optimize restoration models via pixel-based loss functions. Since the seminal super-resolution work of Dong et al. [23], many image super-resolution approaches [54, 53, 47, 50, 75, 58, 71, 43] have adopted an end-to-end neural network to learn the regression model for reconstruction. Recently, attention [73] has also been utilized in image super-resolution to involve more pixels for nonlocal pattern exploration. For example, SwinIR [50] proposes to use Swin Transformer [51] for multi-scale nonlocal feature matching, HAN [58] proposes to combine spatial- and channel-wise attention to model the holistic interdependencies among layers and HAT [20] activates more pixels for high-frequency detail reconstruction via window-based and channel attention. To overcome the bottleneck of information loss caused by the deep attention layers, [41] proposes dense-residual connections to mitigate the spatial loss and stabilize the information flow. Generative adversarial networks [34] point to a new direction of photorealistic image super-resolution, where the model learns the manifold of natural images to produce images with pleasant visual quality. SRGAN [47] and ESRGAN [77] are two efficient approaches that can generate super-resolved images with fine details. Following this direction, a lot of works have been exploring denoising diffusion probabilistic model (DDPMs) [67], score-based models [68], and their recent variations [69, 9, 65, 40, 60] for generative image super-resolution. SR3 [61] and StableSR [75] are two representative approaches that achieve photorealistic image reconstruction. However, they also suffer from high computational costs and slow inference.

Unlike image super-resolution, video super-resolution requires solving spatiotemporal reconstruction such that the resultant video has high visual quality and seamless motion changes. Temporal alignment plays an important role in temporal interpolation and frame enhancement. Optical flow is one effective approach that can estimate the motions between images and perform warping. Without knowing the ground truth optical flow, TOFlow [80] proposes a trainable motion estimation module to predict the motion for video super-resolution. DUF [43] and TDAD [71] propose implicit motion estimation via dynamic upsampling filters and deformable alignment networks. EDVR [76] proposes to learn attention-based pyramid deformable convolution layers for motion estimation and then fuse multiple frames for super-resolution. Another attention-based video SR is [49], which encodes video frames as patch tokens and learns spatiotemporal correlation and warping for better reconstruction. Similar to image super-resolution, there are also some developments in using the diffusion model for video enhancement. [86] proposes a training-free flow-guided recurrent module to explore latent space super-resolution. Allowing text prompts to guide texture creation can balance restoration and generation.

With these advances in deep learning-based super-resolution (SR), its application to climate and weather prediction has gained significant attention, namely climate/weather downscaling. That is, downscaling the grid size for ocean and weather simulation so we can get fine-resolution visualization. For example, it can be used in the sea surface temperature (SST) for high-resolution air-sea interaction study [29, 45]. It can also find the links between coarse sea surface height (SSH) and high-resolution SST fields [70, 82], which can help to understand ocean circulation and sea surface topography. Several works [3, 12, 38, 57] have explored downscaling spatial resolution from 50~100 km to 1~25 km for climate data, and improving temporal resolution to hourly data. This enables more accurate regional infrastructure planning, resource adequacy evaluation, and risk assessment.

### *3.2. Physics-informed downscaling/super-resolution*

Thanks to the great success in image and video super-resolution, considerable studies exist about the interplay between physics and machine learning. The main trend is to approximate the HR data representation based on potentially noisy and under-resolved simulations, like smoke [8], climate [3, 13], and chemistry [33, 74]. Most deep learning-based SR for scientific data can

be categorized into two groups: spatial downscaling and temporal downscaling. For the former, it is similar to image super-resolution where, given the LR data representation, the network should produce fine-grained data representation. For example, Fukami et al. [30] use the SRCNN [23] model to upsample 2D laminar cylinder flow. MeshfreeFlowNet [42] is proposed to reconstruct the turbulent flow in the Rayleigh-Benard problem via a UNet structure. Given the challenge in the laminar finite-rate-chemistry flows, [14] proposes to use PIESRGAN to estimate the high-resolution flow. Using subgrid turbulent flow models, the idea is to extend ESRGAN [77] to the 3D space. Two physics-informed losses, gradient loss and continuity loss, contribute to the gradient and total mass changes. PINNSR proposes to use RRDB blocks [85] to build a GAN-like network to simulate the fine-grid Rayleigh-Taylor instability. The physical loss is used to govern the advection-diffusion process. PhySR [59] proposes to use a physics-informed network to learn temporal downscaling. The key idea is to use ConvLSTM [64] to learn temporal refinement and dynamic evolution on LR features. Stacked residual blocks are used to learn pixel reconstruction. PhySRNet [6] proposes an unsupervised learning approach to approximate the high-resolution counterparts without requiring labeled data.

Similarly, Gao et al. [31] also propose using conservation laws and boundary conditions of fluid flows so that the model can be optimized in a self-supervised manner. Teufel et al. [7] propose to predict fine-grid regional climate simulations via an FSR network, which can learn temporal interpolation via flow warping. [66] modifies the diffusion model to simulate the computational fluid dynamics data. It is trained only on high-resolution to learn multi-scale downsampling scenarios, resulting in a robust downscaling model for 2D turbulent flow estimation. Distinct from existing methods, ours focuses on spatiotemporal downscaling and explicitly explores the multidimensional signal via a spatiotemporal attention module. We also explore physics-informed loss to govern the optimization process and show significant improvements compared to others.

It is worth noticing that applying deep neural networks to the real physical world must produce results that guarantee conservation of key physical quantities such as mass or energy over long simulation time intervals. For instance, given paired LR and HR image pairs, the sum of values at local HR pixels needs to match with corresponding LR pixels. In deep neural networks, the common solution is using physics-informed losses. For example, Beucler et al. [11] propose soft penalties on the loss terms to emulate the

cloud process, so that the network follows the conservation of enthalpy, the conservation of mass, terrestrial radiation, and solar radiation. The high intrinsic uncertainty of the climate system makes it difficult for neural networks to predict long-term simulations. Harder et al. [37] propose a correction layer attached to the neural network and train it via physical data generated by the aerosol microphysics model. It guarantees perfect mass conservation and significant speedup. To better preserve the physical quantities, [38] proposes multiple local average pooling constraints to supervise the training optimization, hence it can have zero violation of the physics, produce no negative pixels, and preserve mass up to numerical precision. In contrast to all the above methods, we propose to use a numerical base method that guarantees the conservation of mass and momentum and conducts downscaling concerning the results of this method. Thus, we guarantee that mass and momentum are conserved over time and enable reliable long-term simulations.

## 4. Approach

This section introduces our workflow, which includes the coastal ocean simulation and the proposed downscaling neural network.

### 4.1. Problem setup for coastal simulation

Given a specific coastal region that we want to model, we first use our DG-based SWE model code for hydrodynamics simulation. Each coastal region is simulated with varying polynomial approximation orders, mesh resolutions, and time steps to capture different levels of detail and accuracy. The simulations are then rendered as images to facilitate the neural network training, leveraging the spatial structure of the data. Specifically, we convert the simulations into three views: the horizontal depth-integrated velocity field  $(U, V)$  and the water elevation  $(\xi)$ , stacking them as RGB channels to create a comprehensive visual representation of the ocean dynamics. For each resolution, we employ three different modes of grid interpolation to examine the impact of interpolation methods on the simulation accuracy and neural network training effectiveness. These simulations at varying spatial and temporal resolutions are utilized for neural network training to enhance the model’s ability to generalize across different scales and time frames.

### 4.2. Proposed DNNCS for coastal downscaling

In Figure 2, we show the overall structure of our proposed DNNCS. Given the input coarse simulation data  $\mathbf{X} \in \mathbb{R}^{T \times H \times W \times C}$ , where T is the number

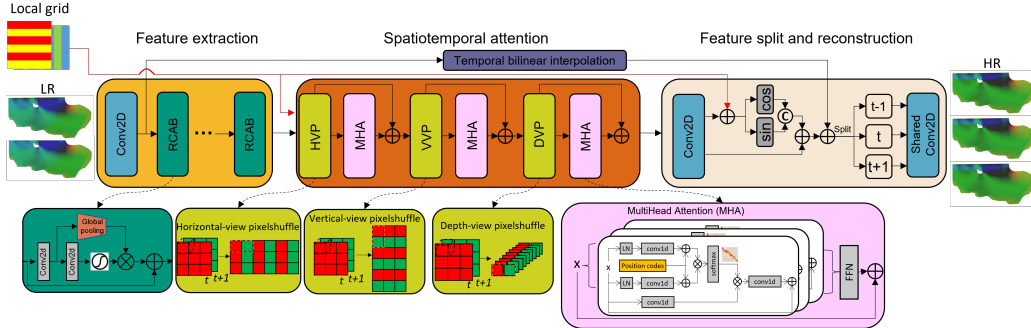


Figure 2: **The overall structure of the proposed DNNCS.** We show the complete architecture of our proposed DNNCS. Given two consecutive coastal simulations, we take them as input to first extract the deep feature representation via multiple RCAB blocks. Then we use spatiotemporal attention to learn the pixel correlations across space and time. Finally, we split the features into three channels for temporal interpolation and spatial downscaling.

of adjacent views,  $H$  and  $W$  are the height and width, and  $C = 3$  is the  $U$ ,  $V$ ,  $\xi$  planes. The proposed DNNCS learns the mapping function  $f: \mathbf{X} \rightarrow \mathbf{Y}$ , where  $\mathbf{Y} \in \mathbb{R}^{\alpha T \times H \times W \times C}$  is the high-resolution coastal estimation, and  $\alpha$  is the temporal upsampling factor. Note that we do not change the spatial resolution because the low-resolution and high-resolution coastal images are rendered from the graph with the same scale but with coarse and fine mesh resolutions, respectively. That is, the resolution of the simulation video does not change, but it becomes more detailed. Inside the network are three key components: Feature extraction, Spatiotemporal attention, and Feature split and reconstruction. Let us introduce them in detail. We train DNNCS on the Bahamas dataset at different downscaling scenarios, and then fine-tune it on the Galveston dataset. The detail of the proposed Bahamas and Galveston datasets will be introduced in Section 5.1

#### 4.3. Feature extraction

The backbone of the feature extraction is based on the Residual Channel Attention Network (RCAN) [84], which takes the adjacent coarse inputs and jointly learns the spatial feature maps as,

$$\mathbf{Z} = \sigma(W_2(W_1(\mathbf{X}))) \times GP(W_1(\mathbf{X})) + \mathbf{X} \quad (2)$$

where  $\mathbf{Z}$  is the extracted feature,  $W_1$  and  $W_2$  are learnable 2D convolutional

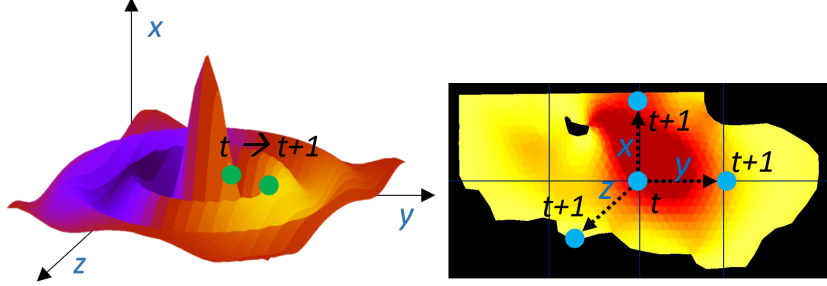


Figure 3: **The spatiotemporal correlation of the water movement.** We visualize the water movement as a 3D heatmap, and we can see that the particle at the same coordinate can relate to neighborhood particles and to itself in the next step.

parameters,  $\sigma$  is the sigmoid function and  $GP$  is the global pooling operation. We stack multiple such RCAN blocks to learn deep feature representation.

#### 4.4. Spatiotemporal attention

The key component of the DNNCS is the spatiotemporal attention. Our goal is to jointly super-resolve the coarse coastal images spatially and temporally. PDEs typically govern spatiotemporal dynamical systems. Let us first consider a simplified wave equation as

$$\frac{\partial^2 u}{\partial t^2} = c^2 \left( \frac{\partial^2 u}{\partial x^2} + \frac{\partial^2 u}{\partial y^2} + \frac{\partial^2 u}{\partial z^2} \right) \quad (3)$$

where  $c$  is a fixed, positive real coefficient, and  $u$  is the scalar displacement field. We can observe that the displacement acceleration is related to the spatial changes around the neighborhood. Inspired by this observation, we design the spatiotemporal attention that transfers the temporal changes across two adjacent frames to the spatial displacement. As shown in Figure 3, the particle at coordinate  $(i, j, k)$  can move in any direction ( $x$ -,  $y$ -, or  $z$ -axis) from time  $t_n$  to  $t_{n+1}$ . Hence, we can use Pixel shuffle to conduct the sub-pixel processing in horizontal, vertical, and depth dimensions.

Mathematically, we can describe the process as

$$H(\mathbf{Z}) = \mathbf{Z} + G(r_h(\mathbf{Z}) + t_h(\mathbf{p})), \quad (4a)$$

$$V(\mathbf{Z}) = H(\mathbf{Z}) + G(r_v(H(\mathbf{Z})) + t_v(\mathbf{p})), \quad (4b)$$

$$D(\mathbf{Z}) = V(\mathbf{Z}) + G(r_d(V(\mathbf{Z})) + t_d(\mathbf{p})), \quad (4c)$$

where  $r_{\{h,v,d\}}$  is the horizontal, vertical, and depth pixel shuffle operator. It fuses the  $t_n$ -th and  $t_{n+1}$ -th wave equation features into one spatiotemporal map.  $H(\cdot)$ ,  $V(\cdot)$  and  $D(\cdot)$  are the corresponding spatial maps that fuse the temporal features along the three dimensions.  $G(\cdot)$  is the MultiHead Attention (MHA) operation. The learnable parameters are shared across horizontal-, vertical- and depth-view computation, which can find the non-local correlations across space and time. As shown in Figure 3, we fuse the features at adjacent frames to calculate the correlations among different directions. In order to record the pixel positional information, we propose to use learnable positional codes  $\mathbf{p}$  to record the relative feature positions and attach them to the corresponding feature maps for computation.

MultiHead Attention (MHA) is a standard nonlocal feature extraction that groups feature maps into subsets and computes the attention map in each subset in parallel. Let us denote the input feature as  $X$ ; we describe the MHA process as,

$$\begin{aligned}
 Y &= FFN(MHA(X)) + X \\
 MHA(X) &= X + \text{Concat}(head_1, head_2, \dots, head_n)W_O \\
 head_i &= \text{softmax}\left(\frac{LN(W_Q(X))LN(W_K(X))}{\sqrt{d}}\right)W_V(X)
 \end{aligned} \tag{5}$$

where *Concat* concatenates the subset of features into one,  $W_{\{Q,K,V\}}$  are query, key and value matrices. *LN* is the layer normalization process, *FFN* is the feed-forward network with multiple convolution layers for the attention output, and  $d$  is the dimension of the feature map, which is used for normalization.

#### 4.5. Feature split and reconstruction

In the feature split and reconstruction process, we first project the learned features into the frequency domain using cosine and sine operators<sup>1</sup>, then combine these components to enhance the original features. We subsequently apply a simple convolution layer to extend these features and split them into three subsets, each representing one of the three temporal feature maps for the coastal data. The input consists of two low-resolution coastal images, with the proposed network (DNNCS) tasked with predicting the intermediate

---

<sup>1</sup>Note that we use cosine and sine operators for computational efficiency as they are used often in image/video coding to capture high-frequency details.

image. To achieve this, we use bilinear interpolation for temporal frame interpolation on the initial feature maps. A short connection is implemented to ensure that the spatiotemporal attention mechanism effectively learns the residuals. Finally, a shared convolution operation is employed to directly output the predicted downscaling coastal images. This approach ensures that the model captures both spatial and temporal details, producing high-quality intermediate frames.

#### 4.6. Losses for coastal downscaling

To train the proposed DNNCS, we propose utilizing three loss terms to better constrain the visual consistency in space and time, including MAE (Mean Absolute Errors) loss,  $L_p$  loss, and physics-informed loss. Given the ground truth and estimated downscaling results  $\mathbf{Y}, \mathbf{Y}' \in \mathbb{R}^{\alpha T \times H \times W \times C}$ , we first have the MAE loss as,

$$L_{mae} = \frac{1}{H \times W \times C \times T} \sum_i^H \sum_j^W \sum_k^C \sum_t^T |Y_{i,j,k}(t) - Y'_{i,j,k}(t)| \quad (6)$$

We also need to compute the  $L_p$  loss as a batch-wise weighted loss function that can balance the sample reconstruction quality. Mathematically we have,

$$L_{lp} = \frac{1}{H \times W \times C \times T} \sum_i^H \sum_j^W \sum_k^C \sum_t^T \frac{\|Y_{i,j,k}(t) - Y'_{i,j,k}(t)\|^2}{\|Y(t)\|^2} \quad (7)$$

Finally, we propose to use differential loss to compute the first-order gradient differences between ground truth and estimations. The idea is to calculate the gradient along horizontal and vertical directions. In the meantime, we also calculate the gradient along the z-axis, which represents the U-, V-, and  $\xi$ -planes.

$$L_{diff} = \left\| \frac{dY(t)}{dx} - \frac{dY'(t)}{dx} \right\|^2 + \left\| \frac{dY(t)}{dy} - \frac{dY'(t)}{dy} \right\|^2 + \left\| \frac{dY(t)}{dz} - \frac{dY'(t)}{dz} \right\|^2 \quad (8)$$

The total loss is defined as the weighted sum of all three losses as  $L = \alpha_{mae} L_{mae} + \alpha_{lp} L_{lp} + \alpha_{of} L_{diff}$ . In our experiments, we set  $\alpha_{mae} = 4, \alpha_{lp} = 1, \alpha_{diff} = 100$  to balance their contributions to the network optimization.

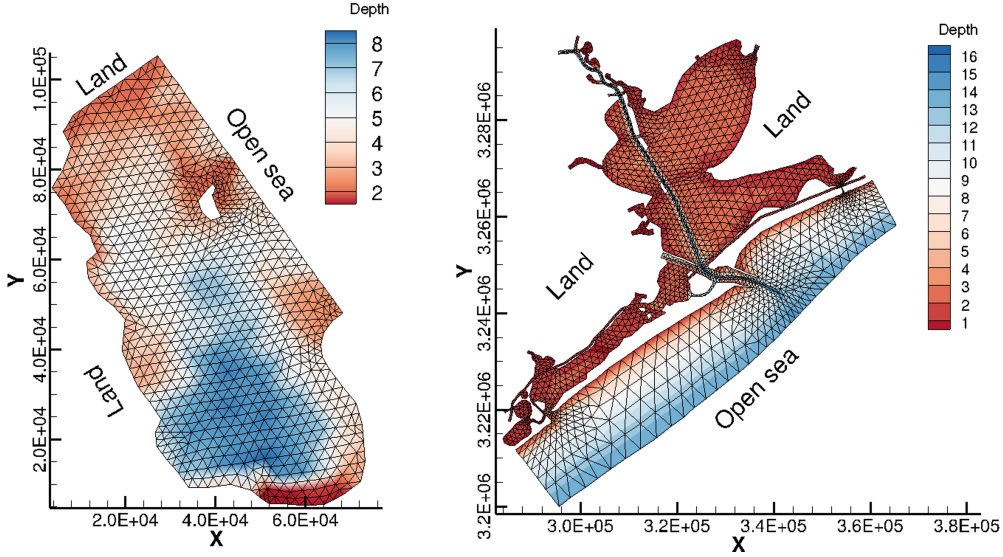


Figure 4: Computational domain, bathymetry (in meters), and the coarse mesh for Bahamas (left, 1696 elements) and Galveston (right, 3397 elements) test cases. The x-axis points East and the y-axis points North.

## 5. Experiments

### 5.1. Implementation Details

**Datasets.** To generate sufficient data samples for model training and analysis, we use UTBEST [1] to simulate the tidal circulation in two locations: Bahamas (Bight of Abaco) and Galveston Bay. The geometry of both computational domains, bathymetry (bottom topography), and the coarsest computational meshes are illustrated in Figure 4. Finer meshes were obtained by subdividing each triangle into four via edge bisection, whereas the bathymetry on finer meshes was obtained by linear interpolation from the coarser mesh nodes to preserve the consistency of problem setup.

At the open sea boundary, both test problems use the tidal elevation consisting of five constituents prescribed by the function

$$\begin{aligned} \hat{\xi}(t) = & 0.075 \cos\left(\frac{t}{25.82} + 3.40\right) + 0.095 \cos\left(\frac{t}{23.94} + 3.60\right) \\ & + 0.1 \cos\left(\frac{t}{12.66} + 5.93\right) + 0.395 \cos\left(\frac{t}{12.42}\right) + 0.06 \cos\left(\frac{t}{12.00} + 0.75\right) \end{aligned} \quad (9)$$

with time  $t$  in hours and use a quadratic bottom friction  $\tau_{bf} = C_f |\mathbf{q}| / H^2$  with  $C_f = 0.009$  (Bahamas) and  $C_f = 0.004$  (Galveston). The Coriolis parameter for Bahamas and Galveston is set to  $3.19 \times 10^{-5} \text{ s}^{-1}$  and  $7.07 \times 10^{-5} \text{ s}^{-1}$ , respectively (see [1] for a more detailed description of the test problems).

The simulations are run for 24 hours with the time step for the lowest approximation order (piecewise constant DG spaces) and the lowest mesh resolution set to 20s for the Bahamas and 12s for the Galveston dataset. Output files with the water height  $\xi$  and depth-integrated horizontal velocities  $U$  and  $V$  are generated in each time step for all configurations. Increasing the mesh resolution or the polynomial discretization order requires smaller time steps (we halve the time step for each mesh refinement and each order increment) and results in more output files. To provide paired LR and HR training data, we consider three levels of downscaling scenarios: size of simulation data, polynomial order of mesh reconstruction and the temporal sampling. Table 1 summarizes the data used for training, with the number of mesh elements shown in “Resolution” and the number of time steps in the “Order” column. We use three approximation orders and resolutions to produce corresponding coarse and fine simulation data at different temporal resolutions. That is, given three approximation orders and three different resolutions, we have a total of  $3 \times 3$  simulation cases for each location. Then, we render all data of their three views ( $U$ ,  $V$ ,  $\xi$  planes) into grayscale images. Finally, all three views are merged as RGB images as the training data. We train one model on both the Bahamas and Galveston datasets for our evaluation.

Table 1: **Summary of the data used in coastal simulation for Bahamas and Galveston.** The “Resolution” value represents the number of mesh elements. In the “Order” column, we list the number of time steps in the 24-hour simulation for the corresponding polynomial discretization order.

| Bahamas    |         |         |         | Galveston  |         |         |         |
|------------|---------|---------|---------|------------|---------|---------|---------|
| Resolution | Order 0 | Order 1 | Order 2 | Resolution | Order 0 | Order 1 | Order 2 |
| 1696       | 4320    | 8640    | 17280   | 3397       | 1800    | 3600    | 7200    |
| 6784       | 8640    | 17280   | 34560   | 13588      | 3600    | 7200    | 14400   |
| 27136      | 17280   | 34560   | 69120   | 54352      | 7200    | 14400   | 28800   |

We randomly split the data into training, validation, and testing in 6 : 2 : 2 ratios without overlapping. The rendered images are of identical dimensions, approximately  $900 \times 500$  pixels. We also mask out the land area

and only focus on the water-covered subdomain downscaling. In the training phase, we learn  $4\times$  spatial downscaling and  $2\times$  temporal downscaling across different orders. We randomly select two adjacent LR coastal images  $(\mathbf{X}(t_n), \mathbf{X}(t_{n+1}))$  from lower resolutions to predict three corresponding HR images  $\mathbf{Y}(t_{2n}), \mathbf{Y}(t_{2n+1}), \mathbf{Y}(t_{2n+2})$  from next higher-resolution. Then we crop the image pairs as patches of size  $64\times 64$ . We randomly apply horizontal & vertical flips, rotations, and frame reversal for data augmentation.

**Parameter setting.** We train DNNCS using Adam optimizer with the learning rate of  $1\times 10^{-4}$ . The learning rate is halved after 30k iterations. The batch size is set to 24, and DNNCS is trained for 100k iterations (about 16 hours) on a PC with one NVIDIA V100 GPU using the PyTorch deep learning platform.

**Metrics and evaluation.** We evaluate different models separately for two scenarios: Bahamas and Galveston. In each scenario, we average the model predictions at different orders. We use five metrics for evaluation:

- **MSE** (Mean Squared Error) and **MAE** (Mean Absolute Error) measure the average pixel differences between ground truth and estimation
- **SSIM** [78] measures the structural similarity between ground truth and estimation
- **GMSD** [81] measures the gradient differences for perceptual quality assessment
- **LPIPS** [83] measures the perceptual similarity between ground truth and estimation

To measure the model complexity, we use FLOPs, memory, and the number of parameters to compare the computation efficiency.

### 5.2. Comparison of the spatiotemporal downscaling with state-of-the-art methods

To show the efficiency of our proposed method, we compare it with four state-of-the-art image super-resolution methods: VDSR [46], RDN [85], StableSR [75] and SwinIR [50], two video super-resolution methods: EDVR [76] and VRT [49], and one physics-informed downscaling method: PhySR [59]. Note that image super-resolution cannot conduct frame interpolation, so we

apply spatiotemporal Bicubic to interpolate the missing frames and then apply frame-by-frame downscaling. All approaches are reimplemented using the publicly available codes, and the methods marked with \* indicate that they were retrained from our coastal dataset for a fair comparison. In Table 2, both Galveston and Bahamas have two downscaling schemes. The “Resolution” column lists the number of grid elements. The result for each scheme is the average of all three polynomial approximation orders. We can see that our approach achieves the best performance with respect to the RMSE, MAE, SSIM, and GMSD metrics and is the second-best in LPIPS.

Table 2: **Comparison with state-of-the-art methods on coastal downscaling.** We report the deviations from the ground truth given by the highest accuracy simulations for the test datasets of Bahamas and Galveston using different metrics.

| Dataset   | Resolution  | Method | ST-Bicubic | VDSR* | RDN*  | ResShift | SwinIR | EDVR* | VRT   | PhySR* | Ours  |
|-----------|-------------|--------|------------|-------|-------|----------|--------|-------|-------|--------|-------|
| Bahamas   | 1696×6784   | RMSE↓  | 0.077      | 0.079 | 0.054 | 0.066    | 0.045  | 0.036 | 0.067 | 0.084  | 0.028 |
|           |             | MAE↓   | 0.035      | 0.033 | 0.023 | 0.041    | 0.026  | 0.014 | 0.038 | 0.036  | 0.011 |
|           |             | SSIM↑  | 0.964      | 0.960 | 0.971 | 0.977    | 0.975  | 0.979 | 0.978 | 0.966  | 0.981 |
|           |             | GMSD↓  | 0.0413     | 0.045 | 0.046 | 0.046    | 0.045  | 0.038 | 0.047 | 0.040  | 0.033 |
|           |             | LPIPS↓ | 0.108      | 0.118 | 0.125 | 0.133    | 0.122  | 0.119 | 0.135 | 0.113  | 0.100 |
|           | 6784×27136  | RMSE↓  | 0.040      | 0.004 | 0.021 | 0.023    | 0.020  | 0.015 | 0.024 | 0.051  | 0.014 |
|           |             | MAE↓   | 0.0208     | 0.018 | 0.009 | 0.010    | 0.007  | 0.007 | 0.011 | 0.022  | 0.006 |
|           |             | SSIM↑  | 0.979      | 0.975 | 0.987 | 0.988    | 0.987  | 0.989 | 0.988 | 0.979  | 0.990 |
|           |             | GMSD↓  | 0.019      | 0.039 | 0.026 | 0.025    | 0.024  | 0.020 | 0.027 | 0.037  | 0.011 |
|           |             | LPIPS↓ | 0.097      | 0.105 | 0.105 | 0.112    | 0.107  | 0.106 | 0.114 | 0.099  | 0.093 |
| Galveston | 3250×13000  | RMSE↓  | 0.039      | 0.020 | 0.021 | 0.023    | 0.024  | 0.009 | 0.023 | 0.032  | 0.007 |
|           |             | MAE↓   | 0.002      | 0.012 | 0.007 | 0.012    | 0.014  | 0.010 | 0.011 | 0.011  | 0.002 |
|           |             | SSIM↑  | 0.972      | 0.990 | 0.989 | 0.989    | 0.989  | 0.988 | 0.990 | 0.988  | 0.996 |
|           |             | GMSD↓  | 0.043      | 0.023 | 0.036 | 0.037    | 0.035  | 0.033 | 0.035 | 0.029  | 0.014 |
|           |             | LPIPS↓ | 0.108      | 0.046 | 0.033 | 0.040    | 0.027  | 0.027 | 0.037 | 0.026  | 0.016 |
|           | 13000×54000 | RMSE↓  | 0.620      | 0.050 | 0.030 | 0.032    | 0.030  | 0.028 | 0.034 | 0.041  | 0.018 |
|           |             | MAE↓   | 0.016      | 0.016 | 0.010 | 0.014    | 0.010  | 0.009 | 0.012 | 0.014  | 0.005 |
|           |             | SSIM↑  | 0.979      | 0.981 | 0.984 | 0.986    | 0.986  | 0.986 | 0.987 | 0.984  | 0.991 |
|           |             | GMSD↓  | 0.079      | 0.059 | 0.049 | 0.047    | 0.047  | 0.049 | 0.041 | 0.045  | 0.035 |
|           |             | LPIPS↓ | 0.079      | 0.048 | 0.043 | 0.048    | 0.045  | 0.043 | 0.040 | 0.038  | 0.028 |

Visually, we report the downscaling results of different methods in Figure 5 for the Bahamas dataset and in Figure 6 for the Galveston Bay. Each plane is normalized between  $[0, 255]$  and shown as a single-channel grayscale

image, and we also stack normalized three planes  $U, V, \xi$  in order as RGB images. In Figure 5, the last row shows the ground truth. Denoting the simulation output for the  $n$ -th time step by  $t_n$ , we show the results for  $t_{15}$  in the first column and the residual maps of  $U$ -,  $V$ - and  $\xi$ -planes between predictions and ground truth in columns 2, 3 and 4, respectively. The last column illustrates the residual maps between  $t_{15}$  and  $t_{30}$  to visualize the temporal changes. We can observe that 1) VDSR, RDN, EDVR, and PhySR wrongly predict the  $V$ -plane simulations, ST-Bicubic, SwinIR, and VRT mispredict the  $U$ -plane simulations, ResShift fails on both  $U$ - and  $\xi$ -planes. We can better minimize the simulation differences simultaneously for  $U$ -,  $V$ - and  $\xi$ -planes. 2) From the last column, we can see that ours can better match with the ground truth changes, while others produce large errors. In Figure 6 of the downscaling results on Galveston Bay (here, the ground truth is shown in the last column), we use white arrows to highlight the significant differences. We can see that 1) globally, ResShift and VRT enlarge the errors caused by ST-Bicubic (the green areas around the boundaries at time  $t_{61}$ ). EDVR produces the wrong pattern at time  $t_{41}$ . 2) From the enlarged areas, we can see that ours can better mimic the changes of the solution around the corners. Others, like VDSR and PhySR\* magnify the zigzag patterns. ResShift and VRT oversmooth the solution which visually causes color shifts.

Three main reasons that other methods fail while ours work: 1) Other image-based approaches (SwinIR, ResShift) are trained with additional perceptual reconstruction losses, which can cause false features or hallucinate detail. 2) Video-based approaches (EDVR, VRT) use estimated optical flow generated by pre-trained neural networks for temporal interpolation. The errors caused by optical flow can be accumulated for spatial downscaling. 3) All other works do not consider physics-informed losses to ensure physical consistency, which would violate the energy flow between frames.

We report the number of parameters, FLOPs, and runtime for model complexity in Table 3. The FLOPs are computed with the input of LR size  $180 \times 180$  and  $\times 4$  upsampling settings. We can see that ours has the third-lowest model complexity regarding the number of parameters and runtime. In general, the model performance and complexity contradict each other. To better visualize the trade-off comparisons among different methods, we summarize the information in Table 2 and Table 3 and visualize them in Figure 7. Ours is located at the bottom left corner, which indicates that it achieves the best balance between model complexity and reconstruction quality.

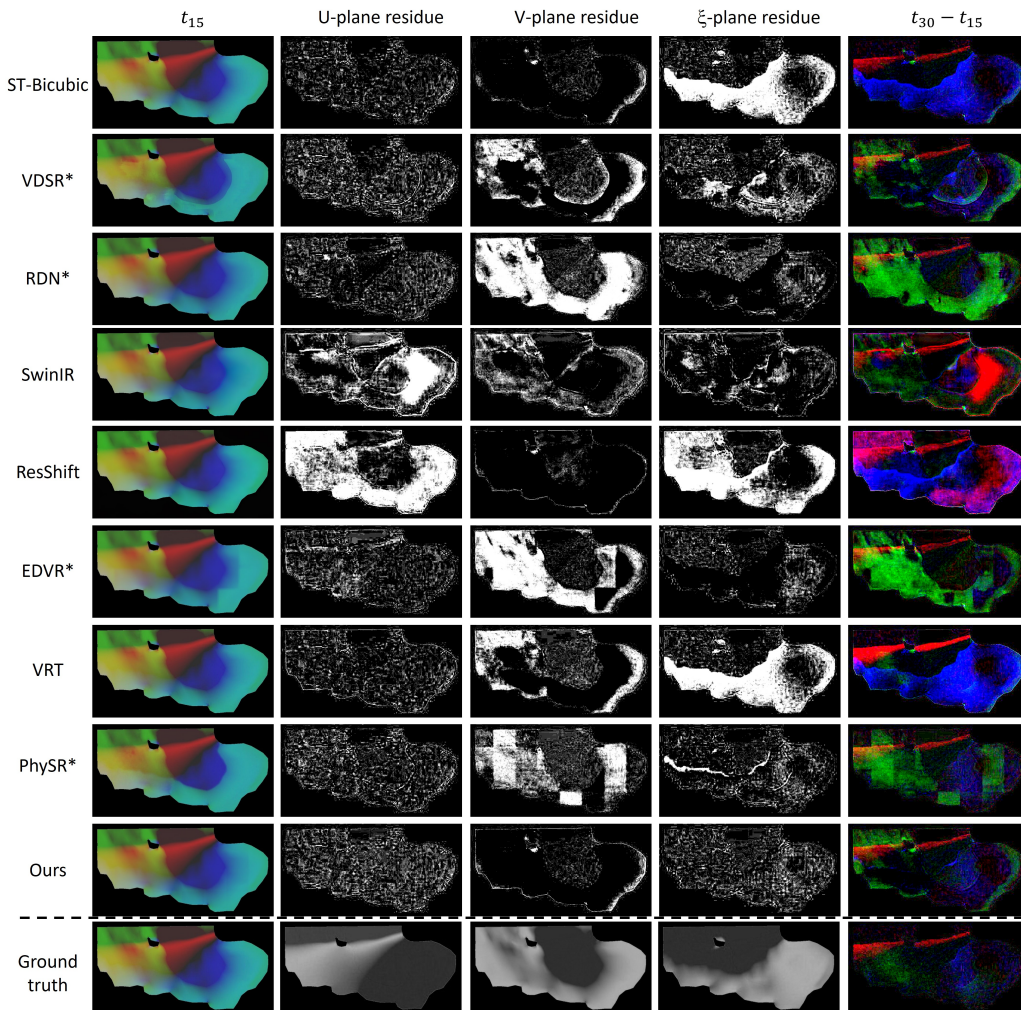


Figure 5: **Visual comparison among different methods on Bahamas dataset.** We show the ground truth from resolution 1696, order 0 at time  $t_{15}$  and  $t_{30}$ , and the corresponding residual maps between prediction and ground truth (U, V, and  $\xi$  planes – we multiply the residuals by factor 50 to highlight the differences), and the residual map between the ground truths at times  $t_{30}$  and  $t_{15}$  (we multiply the residuals by factor 20 for visualization).

### 5.3. Ablation studies and analysis

**Losses for optimization.** We propose to use three loss terms to optimize the proposed model. To show their effects, we visualize their effect by plotting the quantitative metrics in Figure 8. Given LR input at  $t_n$  and  $t_{n+1}$

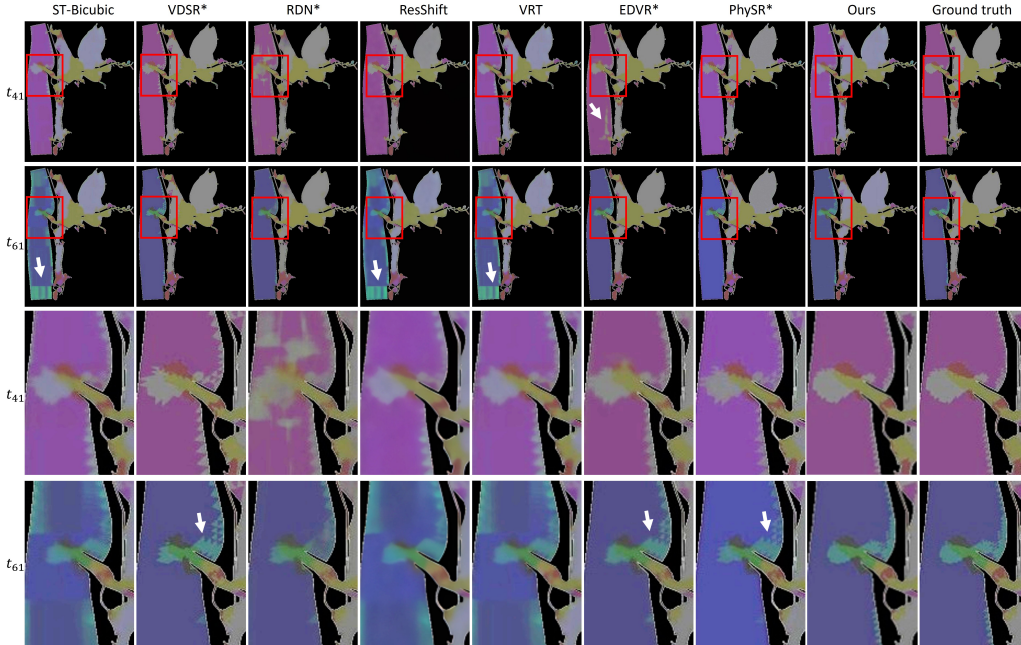


Figure 6: **Visual comparison among different methods on the Galveston dataset.** We use the data sample from resolution 3397, order 1 at time  $t_{41}$  and  $t_{61}$ . The simulation results at time  $t_{41}$  and  $t_{61}$  in RGB images. We enlarge the red box region in rows 3 and 4 to highlight the visual differences.

and the predictions at  $t_{2n}$ ,  $t_{2n+1}$ , and  $t_{2n+2}$ , we take the coastal simulations at  $t_{2n}$  and  $t_{2n+2}$  (we refer to them as intra frames) to compute the spatial differences, and the coastal simulation at  $t_{2n+1}$  (we refer to them as inter frames) to compute the temporal differences. We can see that using  $L_{lp}$  and  $L_{diff}$  losses can reduce both RMSE and MAE losses. Specifically, using  $L_{diff}$  can significantly improve the temporal performance, approximately 24% to 42% in RMSE. It indicates that physics-informed losses can better supervise the temporal consistency for smooth solution changes.

**Key modules for spatiotemporal matching.** There are two key components in our proposed DNNCS: spatiotemporal attention (ST Attn) and feature split and reconstruction (FSR). To illustrate their effects, we use the Bahamas dataset to conduct the ablation studies and report the RMSE, MAE, and SSIM in Table 4. As introduced in Figure 2, the feature extraction module can be any image feature encoders. We choose RDN [85], RCAN [84],

Table 3: **Comparison with state-of-the-art methods on model complexity.** We report the results on the Bahamas dataset under the same hardware settings.

| Method                   | ST-Bicubic | VDSR* | RDN*  | ResShift | SwinIR  | EDVR*  | VRT     | PhySR* | Ours  |
|--------------------------|------------|-------|-------|----------|---------|--------|---------|--------|-------|
| Number of parameters (M) | -          | 0.651 | 21.99 | 118.59   | 11.72   | 20.6   | 35.5    | 0.817  | 8.07  |
| FLOPs (GMac)             | -          | 8.23  | 90.14 | 32156    | 1878.41 | 3020.1 | 3305.75 | 9.20   | 65.15 |
| Runtime (s)              | 0.003      | 0.038 | 0.48  | 15.2     | 4.2     | 1.10   | 2.4     | 0.23   | 1.02  |

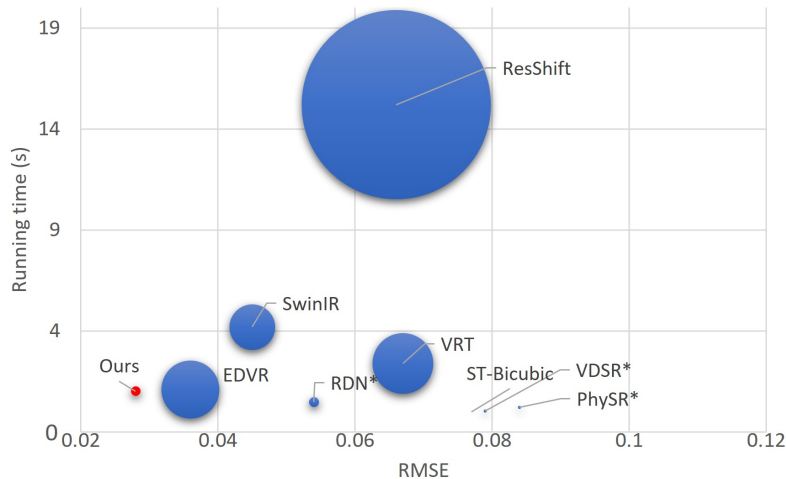


Figure 7: **Speed and performance comparison.** Overall comparison among different methods in terms of speed (runtime on the vertical axis), performance (RMSE on the horizontal axis), and model complexity (size of the bubbles).

and SwinIR [50] as candidates for the feature extraction. Then, we add spatiotemporal attention and/or feature split and reconstruction (FSR) to see if they can positively affect the downscaling performance. We can see that 1) using SwinIR and RCAN is better than RDN as the feature encoder, as they can provide deeper feature representation, and rows 4 and 6 also prove that combining RCAN and spatiotemporal attention and FSR can provide the best performances. 2) Comparing columns 1&4 and 2&5, we can see that spatiotemporal attention can significantly improve the RMSE by about 0.021. Different feature encoders only have 0.08 improvements in RMSE and 0.002 in MAE. Given that SwinIR is a complex and time-consuming model, we choose RCAN, which balances downscaling quality and computation efficiency well.

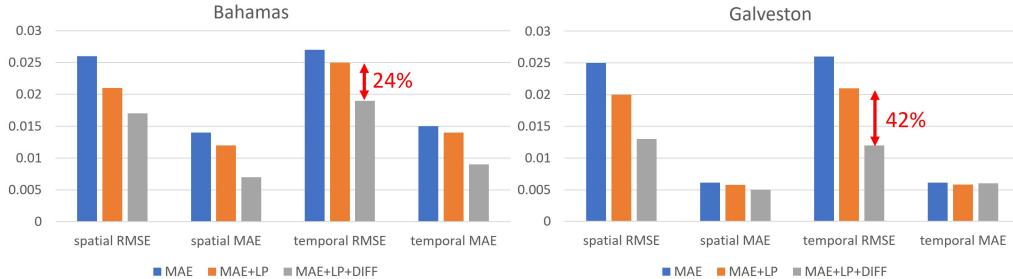


Figure 8: **Quantitative comparisons of using different loss terms.** We show the coastal simulation results on the Bahamas and Galveston by computing the spatial differences (pixel loss on intra frames) and temporal differences (pixel loss on inter frames).

Table 4: **Ablation analysis on the key modules.** We report the results on the test datasets of the Bahamas using different combinations of modules. ST Attn refers to Spatiotemporal attention operation.

| Module     | Feat encoder | RDN   | RCAN  | SwinIR | RDN   | RCAN  | SwinIR | RDN   | RCAN  | SwinIR |
|------------|--------------|-------|-------|--------|-------|-------|--------|-------|-------|--------|
|            | ST Attn      | ✗     | ✗     | ✗      | ✓     | ✓     | ✓      | ✓     | ✓     | ✓      |
|            | FSR          | ✗     | ✗     | ✗      | ✗     | ✗     | ✗      | ✓     | ✓     | ✓      |
| Evaluation | RMSE         | 0.054 | 0.050 | 0.035  | 0.033 | 0.031 | 0.025  | 0.030 | 0.028 | 0.024  |
|            | MAE          | 0.023 | 0.021 | 0.016  | 0.013 | 0.013 | 0.011  | 0.012 | 0.011 | 0.010  |
|            | SSIM         | 0.971 | 0.972 | 0.981  | 0.980 | 0.981 | 0.982  | 0.982 | 0.981 | 0.982  |

**Spatiotemporal attention.** The key module of our proposed DNNCS is the spatiotemporal attention. To visually understand its ability to capture the pixel information for simulation, we use Local Attribution Maps (LAM) [35] to visualize the influences of neighborhood pixels on the region of interest (ROI) in Figure 9. The idea is to calculate the path-integrated gradient along a gradually changing path from the downscaled result to the LR input. In Figure 9, we show the contribution’s pixel attribute map and region in both  $t_n$  and  $t_{n+1}$  LR inputs. The red box region is calculated and enlarged for comparison. We can see that EDVR and ours can explore wider regions, which means that they can extract a wider range of correlated features for calculation. RCAN can also explore larger regions because of its channel attention computation, however, it fails to show the differences caused by the temporal changes. On the contrary, we can observe that ours shows attribu-

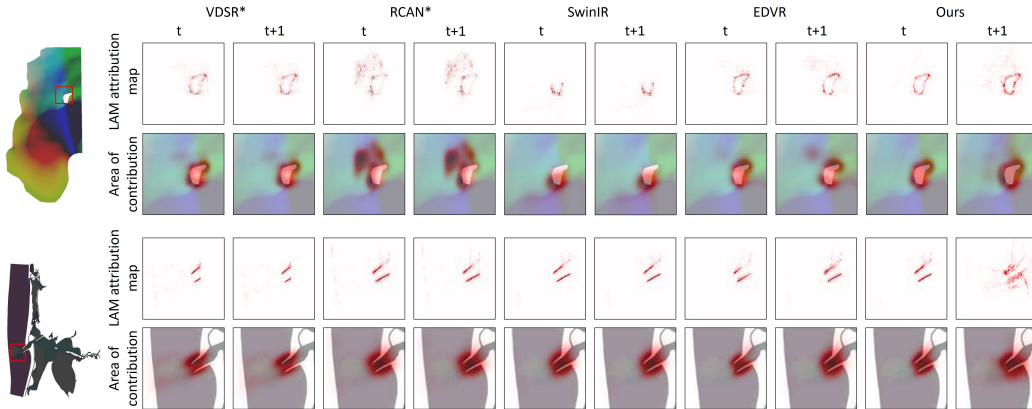


Figure 9: **Interpretation of downscaling method using attribute maps.** The LAM maps represent the importance of each pixel in the input LR image w.r.t. the downscaled results of the patch marked with a red box. We also show the area of contribution to highlight the ROI region for computing feature correlations.

tion changes (the red color ranges become larger from  $t_n$  to  $t_{n+1}$  LR image) because ours can explore the temporal changes and reflect the attention score on the different LR images.

Meanwhile, as introduced in Section III, the proposed spatiotemporal attention explores the horizontal(H)-, vertical(V)- and depth(D)-dimensional feature extraction hence, we conduct the experiments to compare the combination of three sub-attention modules and report the results in Figure 10. On top, we show the RMSE values of using attention operation at different dimensions. “*No attention*” means no attention is used in the network. “*H+V+D+Pos*” means our final model with the positional encoded spatiotemporal attention module. We can conclude that 1) combining horizontal, vertical, and depth attention achieves the best performance, and 2) from the feature maps, we can observe that the module can explicitly capture the dominant feature in corresponding directions.

***Feature split and reconstruction.*** For reconstruction, we are inspired by the recent development of image processing in the frequency domain [48]. We apply the Fast Fourier Transform (FFT) to the LR image and the feature maps to see if they learn different aspects of feature representation. As shown in Figure 11, we show the feature map after cosine and sine operations. The magnitude spectrum maps show that they learn complementary information

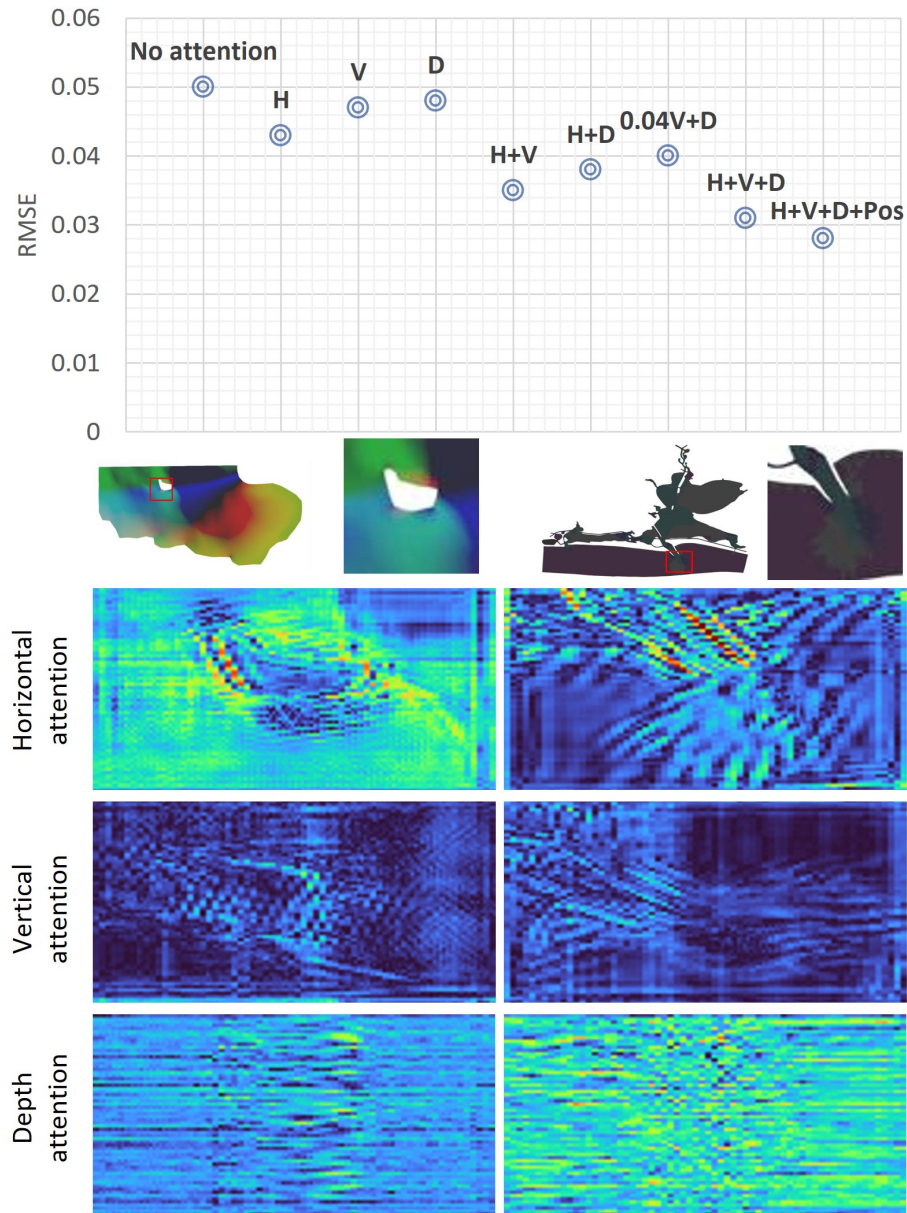


Figure 10: **Visualization of spatiotemporal attention at different dimensions.** On top, we report the RMSE results of using different horizontal, vertical, and depth attention combinations. After applying horizontal, vertical, and depth attention, we show the feature map at the bottom.

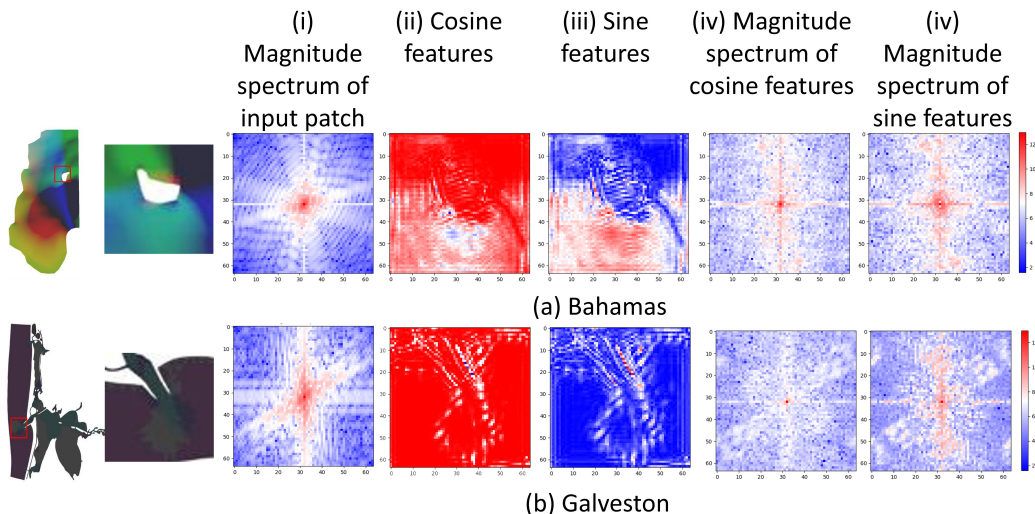


Figure 11: **Visualization of feature split and reconstruction.** We show the heatmap of the magnitude spectrum after applying FFT to the feature maps and the input LR image.

to predict the downscaled result. For instance, the cosine feature map learns the global low-frequency information, and the spectrum energy concentrates in the center. The sine feature map learns more about edge information, and the spectrum energy focuses on the vertical line.

**Motion consistency.** We calculate the RMSE score of the Bahamas dataset to measure the motion consistency. We report intra-frame and inter-frame downscaling results to see if the RMSE score changes due to the spatial and temporal upsampling. We do not use optical flow or other motion estimation models because they are built on key feature point tracking. The figure illustrates RMSE trends over 165 frames for different super-resolution models. Our method (magenta for temporal, red for spatial) exhibits nearly identical curves in both spatial and temporal cases, indicating high motion consistency and robust reconstruction across frames. In contrast, RDN (blue and green) shows a large discrepancy between spatial and temporal RMSE, with noticeable oscillations in the temporal curve, revealing poor temporal coherence. EDVR and PhySR demonstrate smaller spatial-temporal mismatches (the gray and yellow curves of PhySR and light and dark brown curves of EDVR), but both produce higher RMSE overall compared to ours. These

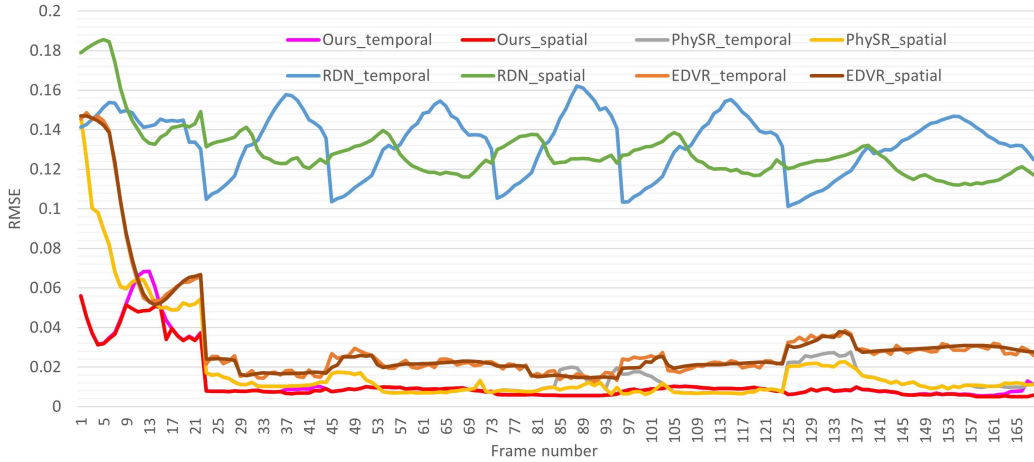


Figure 12: **Plot of frame-by-frame RMSE scores by using different methods.** It compares RMSE across 165 frames for different methods, evaluating spatial and temporal consistency. Temporal RMSE curves for RDN, EDVR and PhySR show prominent oscillations and higher overall error, indicating instability and poor motion coherence across frames. In contrast, spatial RMSE remains relatively flat, suggesting more consistent intra-frame quality. Our method (in pink for temporal and red for spatial) shows rapid convergence within the first 20 frames and maintains the lowest and most stable RMSE afterward, especially in the temporal domain, demonstrating superior consistency over time. There are 8 lines. It is just that some lines are very close to each other. I added some description to the caption and main text.

results highlight that our method achieves the best balance between spatial fidelity and temporal stability, making it particularly suitable for dynamic scenes like coastal simulations where motion preservation is critical.

#### 5.4. Limitations and further discussion

One potential shortcoming of our proposed model is that it should be fine-tuned on other unknown regions for better performance. This is due to the domain-specific physical conditions at different places. For instance, the shoreline can affect fine-grained water movements. In our design, we define the landmass as zero, which serves as a hard condition for the downscaling neural network. One promising approach is to convert the coastal simulation into graphs and use graph neural networks to learn downscaling as graph interpolation. The advantage is that the water movement can pass along the vertices and edges and find nonlocal correlations for downscaling.

## 6. Conclusion

In this paper, we propose DNNCS, a spatiotemporal downscaling neural network for efficient coastal ocean simulation. The proposed spatiotemporal attention fully utilizes the neighborhood pixels across space and time via pixel shuffle to estimate the feature correlations. It can explicitly model the U-, V- and  $\xi$ -view changes over time as spatial feature correlations. The grid location is also embedded as the positional code for axis-aware attention estimation. Finally, we implement the novel feature split and reconstruction to project the features into the frequency domain for final enhancement. The initial spatiotemporal bilinear operator is used to encourage the network to learn the residues between LR and HR data. The proposed physics-informed losses also help to optimize the neural network with better quantitative results. In order to train the neural network, we propose a novel coastal simulation dataset on the Bahamas and Galveston. We use it for model training and evaluation. From extensive experiments and comparisons with other state-of-the-art methods, we can conclude that ours can achieve superior downscaling quality with fast computation.

Since the proposed methodology guarantees the mass conservation for arbitrarily long simulation times, it is particularly attractive for ocean, climate, and weather models for which high resolution simulations are desirable but computationally very expensive. In addition, it paves a novel direction for neural downscaling models for multigrid simulation, and we are interested in further exploration of ultra-resolution reconstruction and continuous downscaling.

## Acknowledgments

A. Rupp has been supported by the Academy of Finland’s grant number 350101 *Mathematical models and numerical methods for water management in soils*, grant number 354489 *Uncertainty quantification for PDEs on hypergraphs*, grant number 359633 *Localized orthogonal decomposition for high-order, hybrid finite elements*, Business Finland’s project number 539/31/2023 *3D-Cure: 3D printing for personalized medicine and customized drug delivery*, and the Finnish *Flagship of advanced mathematics for sensing, imaging and modeling*, decision number 358944. Markus Büttner was partially supported by the German Research Foundation (DFG) under grant AI 117/7-1 within the project 502500606 ‘Performance-optimized co-design of ocean modeling software on FPGAs’.

## References

- [1] Aizinger, V., Dawson, C., 2002. A discontinuous Galerkin method for two-dimensional flow and transport in shallow water. *Advances in Water Resources* 25, 67–84. doi:10.1016/S0309-1708(01)00019-7.
- [2] Aizinger, V., Proft, J., Dawson, C., Pothina, D., Negusse, S., 2013. A three-dimensional discontinuous Galerkin model applied to the baroclinic simulation of Corpus Christi Bay. *Ocean Dynamics* 63, 89–113. doi:10.1007/s10236-012-0579-8.
- [3] et al., R.L., 2023. Learning skillful medium-range global weather forecasting. *Science* 382, 1416–1421.
- [4] Alt, C., Kenter, T., Faghih-Naini, S., Faj, J., Opdenhövel, J.O., Plessl, C., Aizinger, V., et al., 2023. Shallow Water DG Simulations on FPGAs: Design and Comparison of a Novel Code Generation Pipeline, in: *High Performance Computing*, pp. 86–105.
- [5] Androsov, A., Behrens, J., Danilov, S., 2011. Tsunami modelling with unstructured grids. interaction between tides and tsunami waves, in: Krause, E., Shokin, Y., Resch, M., Kröner, D., Shokina, N. (Eds.), *Computational Science and High Performance Computing IV*, Springer Berlin Heidelberg, Berlin, Heidelberg. pp. 191–206.
- [6] Arora, R., 2022. PhySRNet: Physics informed super-resolution network for application in computational solid mechanics, in: *2022 IEEE/ACM International Workshop on Artificial Intelligence and Machine Learning for Scientific Applications (AI4S)*, pp. 13–18. doi:10.1109/AI4S56813.2022.00008.
- [7] B., T., Carmo, F., Sushama, L.e.a., 2023. Physics-informed deep learning framework to model intense precipitation events at super resolution. *Geoscience Letter* 10. doi:10.1186/s40562-023-00272-z.
- [8] Bai, K., Li, W., Desbrun, M., Liu, X., 2020. Dynamic Upsampling of Smoke through Dictionary-based Learning. *ACM Trans. Graph.* 40. doi:10.1145/3412360.

- [9] Bansal, A., Borgnia, E., Chu, H.M., Li, J.S., Kazemi, H., Huang, F., Goldblum, M., Geiping, J., Goldstein, T., 2023. Cold Diffusion: Inverting Arbitrary Image Transforms Without Noise, in: Thirty-seventh Conference on Neural Information Processing Systems. URL: <https://openreview.net/forum?id=XH3ArcCntI>.
- [10] Baptista, M.A., Miranda, J.M., Omira, R., Antunes, C., 2011. Potential inundation of Lisbon downtown by a 1755-like tsunami. *Natural Hazards and Earth System Sciences* 11, 3319–3326. doi:10.5194/nhess-11-3319-2011.
- [11] Beucler, T., Rasp, S., Pritchard, M., Gentine, P., 2019. Achieving Conservation of Energy in Neural Network Emulators for Climate Modeling URL: <https://arxiv.org/abs/1906.06622>, arXiv:1906.06622.
- [12] Bi, K., Xie, L., Zhang, H.e.a., 2023a. Accurate medium-range global weather forecasting with 3D neural networks. *Nature* 619, 533–538. doi:<https://doi.org/10.1038/s41586-023-06185-3>.
- [13] Bi, K., Xie, L., Zhang, H.e.a., 2023b. Accurate medium-range global weather forecasting with 3D neural networks. *Nature* 619, 533–538.
- [14] Bode, M., Gauding, M., Lian, Z., Denker, D., Davidovic, M., Kleinhainz, K., Jitsev, J., Pitsch, H., 2021. Using physics-informed enhanced super-resolution generative adversarial networks for subfilter modeling in turbulent reactive flows. *Proceedings of the Combustion Institute* 38, 2617–2625. doi:<https://doi.org/10.1016/j.proci.2020.06.022>.
- [15] Bui-Thanh, T., 2016. Construction and Analysis of HDG Methods for Linearized Shallow Water Equations. *SIAM Journal on Scientific Computing* 38, A3696–A3719. doi:10.1137/16M1057243.
- [16] Bunya, S., Dietrich, J.C., Westerink, J.J., Ebersole, B.A., et al., 2010. A High-Resolution Coupled Riverine Flow, Tide, Wind, Wind Wave, and Storm Surge Model for Southern Louisiana and Mississippi. Part I: Model Development and Validation. *Monthly Weather Review* 138, 345 – 377.
- [17] Buttinger-Kreuzhuber, A., Konev, A., Horváth, Z., Cornel, D., Schwerdorf, I., Blöschl, G., Waser, J., 2022. An integrated GPU-accelerated

- modeling framework for high-resolution simulations of rural and urban flash floods. *Environmental Modelling & Software* 156, 105480. doi:<https://doi.org/10.1016/j.envsoft.2022.105480>.
- [18] Büttner, M., Alt, C., Kenter, T., Köstler, H., Plessl, C., Aizinger, V., 2024. Enabling Performance Portability for Shallow Water Equations on CPUs, GPUs, and FPGAs with SYCL, in: *Proceedings of the Platform for Advanced Scientific Computing Conference, Association for Computing Machinery, New York, NY, USA*. doi:10.1145/3659914.3659925.
- [19] Büttner, M., Alt, C., Kenter, T., Köstler, H., Plessl, C., Aizinger, V., 2025. Analyzing performance portability for a SYCL implementation of the 2D shallow water equations. *The Journal of Supercomputing* 81. URL: <https://doi.org/10.1007/s11227-025-07063-7>, doi:10.1007/s11227-025-07063-7.
- [20] Chen, X., Wang, X., Zhou, J., Qiao, Y., Dong, C., 2023. Activating More Pixels in Image Super-Resolution Transformer, in: *Proceedings of the IEEE/CVF Conference on Computer Vision and Pattern Recognition (CVPR)*, pp. 22367–22377.
- [21] Cockburn, B., Shu, C.W., 1989. TVB Runge-Kutta local projection discontinuous Galerkin finite element method for conservation laws. II. General framework. *Math. Comp.* 52, 411–435. doi:10.1090/S0025-5718-1989-0983311-4.
- [22] Dawson, C., Aizinger, V., 2005. A discontinuous Galerkin method for three-dimensional shallow water equations. *Journal of Scientific Computing* 22, 245–267. doi:10.1007/s10915-004-4139-3.
- [23] Dong, C., Loy, C.C., He, K., Tang, X., 2016. Image Super-Resolution Using Deep Convolutional Networks. *IEEE Transactions on Pattern Analysis and Machine Intelligence* 38, 295–307. doi:10.1109/TPAMI.2015.2439281.
- [24] Eskilsson, C., Sherwin, S.J., 2004. A triangular spectral/hp discontinuous Galerkin method for modelling 2D shallow water equations. *International Journal for Numerical Methods in Fluids* 45, 605–623. doi:10.1002/flid.709.

- [25] Faghih-Naini, S., Aizinger, V., Kuckuk, S., Angersbach, R., Köstler, H., 2025. p-adaptive discontinuous Galerkin method for the shallow water equations on heterogeneous computing architectures. *GEM : International Journal on Geomathematics* 16. URL: <https://doi.org/10.1007/s13137-025-00267-2>, doi:10.1007/s13137-025-00267-2.
- [26] Faghih-Naini, S., Kuckuk, S., Aizinger, V., Zint, D., Grosso, R., Köstler, H., 2020. Quadrature-free discontinuous Galerkin method with code generation features for shallow water equations on automatically generated block-structured meshes. *Advances in Water Resources* 138, 103552.
- [27] Faghih-Naini, S., Kuckuk, S., Zint, D., Kemmler, S., Köstler, H., Aizinger, V., 2023. Discontinuous Galerkin method for the shallow water equations on complex domains using masked block-structured grids. *Advances in Water Resources* , 104584doi:10.1016/j.advwatres.2023.104584.
- [28] Faj, J., Kenter, T., Faghih-Naini, S., Plessl, C., Aizinger, V., 2023. Scalable Multi-FPGA Design of a Discontinuous Galerkin Shallow-Water Model on Unstructured Meshes, in: *Proceedings of the Platform for Advanced Scientific Computing Conference, Association for Computing Machinery, New York, NY, USA.* doi:10.1145/3592979.3593407.
- [29] Fanelli, C., Ciani, D., Pisano, A., Buongiorno Nardelli, B., 2024. Deep learning for the super resolution of Mediterranean sea surface temperature fields. *Ocean Science* 20, 1035–1050. URL: <https://os.copernicus.org/articles/20/1035/2024/>, doi:10.5194/os-20-1035-2024.
- [30] Fukami, K., Fukagata, K., , Taira, K., 2019. Super-resolution reconstruction of turbulent flows with machine learning. *Journal of Fluid Mechanics* 870, 106–120. doi:10.1017/jfm.2019.238.
- [31] Gao, H., Sun, L., Wang, J.X., 2021. Super-resolution and denoising of fluid flow using physics-informed convolutional neural networks without high-resolution labels. *Physics of Fluids* 33, 073603. doi:10.1063/5.0054312.
- [32] Gerhard, N., Caviedes-Voullième, D., Müller, S., Kesserwani, G., 2015. Multiwavelet-based grid adaptation with discontinuous Galerkin

- schemes for shallow water equations. *Journal of Computational Physics* 301, 265–288. doi:<https://doi.org/10.1016/j.jcp.2015.08.030>.
- [33] Goodall, R.E.A., Lee, A.A., 2020. Predicting materials properties without crystal structure: deep representation learning from stoichiometry. *Nature Communication* 6280.
- [34] Goodfellow, I.J., Pouget-Abadie, J., Mirza, M., Xu, B., Warde-Farley, D., Ozair, S., Courville, A., Bengio, Y., 2014. Generative adversarial nets, in: *International Conference on Neural Information Processing Systems*, p. 2672–2680.
- [35] Gu, J., Dong, C., 2021. Interpreting Super-Resolution Networks with Local Attribution Maps, in: *Proceedings of the IEEE/CVF Conference on Computer Vision and Pattern Recognition*, pp. 9199–9208.
- [36] Hajduk, H., Hodges, B.R., Aizinger, V., Reuter, B., 2018. Locally filtered transport for computational efficiency in multi-component advection-reaction models. *Environmental Modelling & Software* 102, 185–198. doi:[10.1016/j.envsoft.2018.01.003](https://doi.org/10.1016/j.envsoft.2018.01.003).
- [37] Harder, P., Watson-Parris, D., et al., 2022a. Physics-informed learning of aerosol microphysics. *Environmental Data Science* 1, e20. doi:[10.1017/eds.2022.22](https://doi.org/10.1017/eds.2022.22).
- [38] Harder, P., Yang, Q., et al., 2022b. Generating physically-consistent high-resolution climate data with hard-constrained neural networks.
- [39] Hauck, M., Aizinger, V., Frank, F., Hajduk, H., Rupp, A., 2020. Enriched Galerkin method for the shallow-water equations. *GEM : International Journal on Geomathematics* 11. doi:[10.1007/s13137-020-00167-7](https://doi.org/10.1007/s13137-020-00167-7). article number 31.
- [40] Hoogeboom, E., Gritsenko, A.A., Bastings, J., Poole, B., van den Berg, R., Salimans, T., 2022. Autoregressive Diffusion Models, in: *International Conference on Learning Representations*. URL: <https://openreview.net/forum?id=Lm8T39vLDTE>.
- [41] Hsu, C.C., Lee, C.M., Chou, Y.S., 2024. DRCT: Saving Image Super-Resolution Away from Information Bottleneck, in: *Proceedings of the*

IEEE/CVF Conference on Computer Vision and Pattern Recognition (CVPR) Workshops, pp. 6133–6142.

- [42] Jiang, C.M., Esmaeilzadeh, S., Azizzadenesheli, K., Kashinath, K., Mustafa, M., Tchelepi, H.A., Marcus, P., Prabhat, Anandkumar, A., 2020. MeshfreeFlowNet: a physics-constrained deep continuous space-time super-resolution framework, in: Proceedings of the International Conference for High Performance Computing, Networking, Storage and Analysis.
- [43] Jo, Y., Oh, S.W., Kang, J., Kim, S.J., 2018. Deep Video Super-Resolution Network Using Dynamic Upsampling Filters Without Explicit Motion Compensation, in: 2018 IEEE/CVF Conference on Computer Vision and Pattern Recognition, pp. 3224–3232.
- [44] Kenter, T., Shambhu, A., Faghieh-Naini, S., Aizinger, V., 2021. Algorithm-Hardware Co-Design of a Discontinuous Galerkin Shallow-Water Model for a Dataflow Architecture on FPGA, in: Proceedings of the Platform for Advanced Scientific Computing Conference.
- [45] Kim, J., Kim, T., Ryu, J.G., 2023. Multi-source deep data fusion and super-resolution for downscaling sea surface temperature guided by Generative Adversarial Network-based spatiotemporal dependency learning. International Journal of Applied Earth Observation and Geoinformation 119, 103312. doi:<https://doi.org/10.1016/j.jag.2023.103312>.
- [46] Kim, J., Lee, J.K., Lee, K.M., 2016. Accurate Image Super-Resolution Using Very Deep Convolutional Networks, in: 2016 IEEE Conference on Computer Vision and Pattern Recognition (CVPR), pp. 1646–1654. doi:[10.1109/CVPR.2016.182](https://doi.org/10.1109/CVPR.2016.182).
- [47] Ledig, C., Theis, L., Huszár, F., Caballero, J., Cunningham, A., Acosta, A., Aitken, A., Tejani, A., Totz, J., Wang, Z., Shi, W., 2017. Photo-Realistic Single Image Super-Resolution Using a Generative Adversarial Network, in: 2017 IEEE Conference on Computer Vision and Pattern Recognition (CVPR), pp. 105–114. doi:[10.1109/CVPR.2017.19](https://doi.org/10.1109/CVPR.2017.19).
- [48] Lee, J., Jin, K.H., 2022. Local Texture Estimator for Implicit Representation Function, in: Proceedings of the IEEE/CVF Conference on Computer Vision and Pattern Recognition (CVPR), pp. 1929–1938.

- [49] Liang, J., Cao, J., Fan, Y., Zhang, K., Ranjan, R., Li, Y., Timofte, R., Van Gool, L., 2024. VRT: A Video Restoration Transformer. *IEEE Transactions on Image Processing* 33, 2171–2182. doi:10.1109/TIP.2024.3372454.
- [50] Liang, J., Cao, J., Sun, G., Zhang, K., Van Gool, L., Timofte, R., 2021. SwinIR: Image Restoration Using Swin Transformer, in: 2021 IEEE/CVF International Conference on Computer Vision Workshops (ICCVW), pp. 1833–1844. doi:10.1109/ICCVW54120.2021.00210.
- [51] Liu, Z., Lin, Y., Cao, Y., Hu, H., Wei, Y., Zhang, Z., Lin, S., Guo, B., 2021. Swin Transformer: Hierarchical Vision Transformer using Shifted Windows, in: Proceedings of the IEEE/CVF International Conference on Computer Vision (ICCV).
- [52] Liu, Z.S., et al., 2019. Image super-resolution via attention based back projection networks, in: 2019 IEEE/CVF International Conference on Computer Vision Workshop (ICCVW), pp. 3517–3525.
- [53] Liu, Z.S., et al., 2020. Unsupervised real image super-resolution via generative variational autoencoder, in: Proceedings of the IEEE/CVF Conference on Computer Vision and Pattern Recognition (CVPR) Workshops.
- [54] Liu, Z.S., et al., 2021. Photo-realistic image super-resolution via variational autoencoders. *IEEE Transactions on Circuits and Systems for Video Technology* 31, 1351–1365.
- [55] Morales-Hernández, M., Sharif, M.B., Gangrade, S., Dullo, T.T., Kao, S.C., Kalyanapu, A., Ghafoor, S.K., Evans, K.J., Madadi-Kandjani, E., Hodges, B.R., 2020. High-performance computing in water resources hydrodynamics. *Journal of Hydroinformatics* 22, 1217–1235. doi:10.2166/hydro.2020.163.
- [56] Moraru, A., Rütther, N., Bruland, O., 2023. Investigating optimal 2D hydrodynamic modeling of a recent flash flood in a steep Norwegian river using high-performance computing. *Journal of Hydroinformatics* 25, 1690–1712. doi:10.2166/hydro.2023.012.

- [57] Nguyen, T., Brandstetter, J., Kapoor, A., Gupta, J.K., Grover, A., 2023. ClimaX: A foundation model for weather and climate. Conference on Neural Information Processing Systems (NeurIPS) .
- [58] Niu, B., Wen, W., Ren, W., Zhang, X., Yang, L., Wang, S., Zhang, K., Cao, X., Shen, H., 2020. Single Image Super-Resolution via a Holistic Attention Network, in: European Conference on Computer Vision (ECCV2020), p. 191–207.
- [59] Ren, P., Rao, C., Liu, Y., Ma, Z., Wang, Q., Wang, J.X., Sun, H., 2023. PhysSR: Physics-informed Deep Super-resolution for Spatiotemporal Data. *Journal of Computational Physics* , 112438.
- [60] Rombach, R., Blattmann, A., Lorenz, D., Esser, P., Ommer, B., 2022. High-Resolution Image Synthesis with Latent Diffusion Models, in: 2022 IEEE/CVF Conference on Computer Vision and Pattern Recognition (CVPR), pp. 10674–10685. doi:10.1109/CVPR52688.2022.01042.
- [61] Saharia, C., Ho, J., Chan, W., Salimans, T., Fleet, D.J., Norouzi, M., 2023. Image Super-Resolution via Iterative Refinement. *IEEE Transactions on Pattern Analysis and Machine Intelligence* 45, 4713–4726. doi:10.1109/TPAMI.2022.3204461.
- [62] Samii, A., Kazhyken, K., Michoski, C., Dawson, C., 2019. A comparison of the explicit and implicit hybridizable discontinuous Galerkin methods for nonlinear shallow water equations. *Journal of Scientific Computing* 80. doi:10.1007/s10915-019-01007-z.
- [63] Shaw, J., Kesserwani, G., Neal, J., Bates, P., Sharifian, M.K., 2021. LISFLOOD-FP 8.0: the new discontinuous Galerkin shallow-water solver for multi-core CPUs and GPUs. *Geoscientific Model Development* 14, 3577–3602. doi:10.5194/gmd-14-3577-2021.
- [64] Shi, X., Chen, Z., Wang, H., Yeung, D.Y., Wong, W.k., Woo, W.c., 2015. Convolutional LSTM Network: a machine learning approach for precipitation nowcasting, in: Proceedings of the 28th International Conference on Neural Information Processing Systems, Cambridge, MA, USA. p. 802–810.
- [65] Shocher, A., Dravid, A.V., Gandelsman, Y., Mosseri, I., Rubinstein, M., Efros, A.A., 2024. Idempotent Generative Network, in: The Twelfth

International Conference on Learning Representations. URL: <https://openreview.net/forum?id=XIaS66XkNA>.

- [66] Shu, D., Li, Z., Barati Farimani, A., 2023. A physics-informed diffusion model for high-fidelity flow field reconstruction. *Journal of Computational Physics* 478, 111972. doi:<https://doi.org/10.1016/j.jcp.2023.111972>.
- [67] Sohl-Dickstein, J., Weiss, E., Maheswaranathan, N., Ganguli, S., 2015. Deep Unsupervised Learning using Nonequilibrium Thermodynamics, in: Bach, F., Blei, D. (Eds.), *Proceedings of the 32nd International Conference on Machine Learning*, PMLR, Lille, France. pp. 2256–2265.
- [68] Song, Y., Sohl-Dickstein, J., Kingma, D.P., Kumar, A., Ermon, S., Poole, B., 2021. Score-Based Generative Modeling through Stochastic Differential Equations, in: *International Conference on Learning Representations*. URL: <https://openreview.net/forum?id=PXTIG12RRHS>.
- [69] Song, Y., et al., 2023. Consistency Models, in: *Proceeding of International Conference on Machine Learning*.
- [70] Thiria, S., Sorrow, C., Archambault, T., Charantonis, A., Bereziat, D., Mejia, C., Molines, J.M., Crépon, M., 2023. Downscaling of ocean fields by fusion of heterogeneous observations using Deep Learning algorithms. *Ocean Modelling* 182, 102174. doi:<https://doi.org/10.1016/j.ocemod.2023.102174>.
- [71] Tian, Y., Zhang, Y., Fu, Y., Xu, C., 2020. TDAN: Temporally-Deformable Alignment Network for Video Super-Resolution, in: *2020 IEEE/CVF Conference on Computer Vision and Pattern Recognition (CVPR)*, pp. 3357–3366. doi:10.1109/CVPR42600.2020.00342.
- [72] Tumolo, G., Bonaventura, L., 2015. A semi-implicit, semi-Lagrangian discontinuous Galerkin framework for adaptive numerical weather prediction. *Quarterly Journal of the Royal Meteorological Society* 141, 2582–2601. doi:<https://doi.org/10.1002/qj.2544>.
- [73] Vaswani, A., Shazeer, N., Parmar, N., Uszkoreit, J., Jones, L., A. Gomez, I.P., 2017. Attention is all you need, in: *Advances in neural information processing systems*, pp. 5998–6008.

- [74] Volk, A.A., Epps, R.W., Yonemoto, D.T., et al., B.S.M., 2023. AlphaFlow: autonomous discovery and optimization of multi-step chemistry using a self-driven fluidic lab guided by reinforcement learning. *Nature Communication* .
- [75] Wang, J., Yue, Z., Zhou, S., Chan, K.C., Loy, C.C., 2024. Exploiting Diffusion Prior for Real-World Image Super-Resolution, in: *International Journal of Computer Vision*.
- [76] Wang, X., Chan, K.C., Yu, K., Dong, C., Loy, C.C., 2019. EDVR: Video Restoration with Enhanced Deformable Convolutional Networks, in: *The IEEE Conference on Computer Vision and Pattern Recognition (CVPR) Workshops*.
- [77] Wang, X., Yu, K., Wu, S., Gu, J., Liu, Y., Dong, C., Qiao, Y., Loy, C.C., 2018. ESRGAN: Enhanced super-resolution generative adversarial networks, in: *The European Conference on Computer Vision Workshops (ECCVW)*.
- [78] Wang, Z., Bovik, A.C., Sheikh, H.R., Simoncelli, E.P., 2004. Image quality assessment: from error visibility to structural similarity. *IEEE Transactions on Image Processing* 13, 600–612.
- [79] Wichitrnithed, C., Valseth, E., Kubatko, E.J., Kang, Y., Hudson, M., Dawson, C., 2024. A discontinuous Galerkin finite element model for compound flood simulations. *Computer Methods in Applied Mechanics and Engineering* 420, 116707. doi:<https://doi.org/10.1016/j.cma.2023.116707>.
- [80] Xue, T., Chen, B., Wu, J., Wei, D., Freeman, W.T., 2019. Video enhancement with task-oriented flow. *International Journal of Computer Vision (IJCV)* 127, 1106–1125.
- [81] Xue, W., Zhang, L., Mou, X., Bovik, A.C., 2014. Gradient Magnitude Similarity Deviation: A Highly Efficient Perceptual Image Quality Index. *IEEE Transactions on Image Processing* 23, 684–695.
- [82] Yuan, B., Jacob, B., Chen, W., Staneva, J., 2024. Downscaling sea surface height and currents in coastal regions using convolutional neural network. *Applied Ocean Research* 151, 104153. doi:<https://doi.org/10.1016/j.apor.2024.104153>.

- [83] Zhang, R., Isola, P., Efros, A.A., Shechtman, E., Wang, O., 2018a. The unreasonable effectiveness of deep features as a perceptual metric, in: CVPR.
- [84] Zhang, Y., Li, K., Li, K., Wang, L., Zhong, B., Fu, Y., 2018b. Image Super-Resolution Using Very Deep Residual Channel Attention Networks, in: ECCV.
- [85] Zhang, Y., Tian, Y., Kong, Y., Zhong, B., Fu, Y., 2018c. Residual Dense Network for Image Super-Resolution, in: 2018 IEEE/CVF Conference on Computer Vision and Pattern Recognition, pp. 2472–2481. doi:10.1109/CVPR.2018.00262.
- [86] Zhou, S., Yang, P., Wang, J., Luo, Y., Loy, C.C., 2024. Upscale-A-Video: Temporal-Consistent Diffusion Model for Real-World Video Super-Resolution, in: Proceedings of the IEEE/CVF Conference on Computer Vision and Pattern Recognition (CVPR), pp. 2535–2545.